

Silicon-Based Nanorod Anodes by Employing Bacterial Cellulose Derived Carbon Skeleton Towards Lithium-Ion Batteries

Jie Wang,*^[a, b] Jiafeng Gao,^[a] Jian Zhang,^[a] Qiwen Jiang,^[c] Huanhuan Yin,^[a] Ziqi Wang,^[a] and Songlin Zuo*^[a]

Huge volume change and high cost of silicon (Si) during the lithium insertion/extraction processes are still major challenges in practical application of Li-ion batteries (LIBs). Herein, for the first time, a scalable one-dimensional (1D) robust Si/C nanorods are developed by using pyrolytic bacterial cellulose (pBC) as 1D carbon skeleton and introducing carbon dioxide (CO_2) greenhouse gas into traditional magnesiothermic reduction reaction, to accelerate the commercial utilization of Si/C composite electrodes. pBC arrays are generated via a self-assembled parallel arrangement process in the SiO_2/pBC hybrids. Notably, pBC arrays as a strong structural support and CO_2 -derived in-

situ generated amorphous carbon as an ideal encapsulation endow Si/C nanorods with high structure robustness and good electronic conductivity. In particular, Si-based nanorods anodes with carbon component content of 11 wt% deliver high reversible specific capacity, good Coulombic efficiency and impressive cycling performance. Such excellent electrochemical performance is attributed to unique Si/C nanorod structure and its superior properties, which can provide good accommodation of volume changes, superior electrolyte wetting, and fast electrons and lithium ions transportation pathways during charging and discharging processes.

Introduction

Silicon (Si) is the most promising candidate for next-generation lithium-ion batteries (LIBs), owing to its high specific capacity ($\sim 3579 \text{ mAh g}^{-1}$ for $\text{Li}_{15}\text{Si}_4$, ten times that of commercial graphite), low discharge voltage ($< 0.5 \text{ V}$ vs. Li/Li^+), environmental friendliness and natural abundance.^[1–4] The development and application of silicon anode can realize high energy density and thus satisfy the ever-growing demands in the electrical vehicles.^[5] Unfortunately, the wider utilization of silicon for LIBs is hampered by several major drawbacks such as its large volume change ($\sim 400\%$) during lithium ion insertion/extraction processes, low electrical conductivity ($\sim 10^{-3} \text{ S cm}^{-1}$), ionic conductivity ($10^{-14}–10^{-13} \text{ cm}^2 \text{ s}^{-1}$) and high fabrication cost.^[6] Such dramatic volume change induces cracking and pulveriza-

tion of Si and then new generation of solid electrolyte interphase (SEI) films, combined with low intrinsic electronic conductivity, which will cause losses of electrical contact among active materials, conductive additives, binders and current collectors in the electrode, resulting in rapid capacity fading.^[7] To address these challenging issues, and obtain facile strain relaxation and manipulation of volume changes and good electron conductivity, two main strategies are usually applied. One strategy is nano-Si dimensional design (e.g., 0D, 1D, 2D, 3D) from 0D hollow nanospheres,^[8] 1D nanostructures such as nanowires,^[9] nanotubes,^[10,11] and 2D films,^[6,12] to 3D mesoporous Si structures.^[13] Another strategy is to combine Si particles with conductive species such as carbonaceous materials,^[14–16] metal nanoparticles^[17,18] and polymers.^[19,20] To the best of our knowledge, 1D Si nanostructures not only can largely avoid cracking and pulverization of Si because of hoop stress relaxation during the repeated lithium insertion/extraction processes by reducing the thickness or diameter to a few nanometers, but also provide good electrical contact between conductive additives or current substrate and active materials.^[21] Notably, pure Si needs to be less than 250 nm in diameter for 1D nanostructures to avoid mechanical fracture.^[22,23]

Till now, numerous efforts have been made to design 1D Si-based anodes for high-performance LIBs. For one thing, 1D Si-based nanostructures engineering commonly needs soft or hard nanoscale sacrificial templates such as Pluronic F127 block copolymer,^[24] CaCO_3 ,^[25] ZnO ^[26] and polyacrylonitrile (PAN) nanowires.^[27] However, removal of the template always confronts sophisticated reaction procedures and high cost. It is worth noting that 1D carbon [e.g., carbon nanotube (CNT)] has attracted great attention on 1D nano-Si design due to its

[a] Dr. J. Wang, J. Gao, J. Zhang, H. Yin, Z. Wang, Prof. S. Zuo
Jiangsu Co-Innovation Center of Efficient Processing and Utilization of Forest Resources, Jiangsu Key Lab of Biomass Based Green Fuels and Chemicals
College of Chemical Engineering
Nanjing Forestry University
International Innovation Center for Forest Chemicals and Materials
210037 Nanjing, China
E-mail: jiewang@njfu.edu.cn
zslnl@hotmail.com

[b] Dr. J. Wang
Key Laboratory of Electrochemical Energy Storage Technology Enterprises of Jiangsu
Shoto Group Co., LTD, 225300 Taizhou, China

[c] Q. Jiang
Jiangsu Co-Innovation Center of Efficient Processing and Utilization of Forest Resources
Nanjing Forestry University, 210037, Nanjing, China

Supporting information for this article is available on the WWW under
<https://doi.org/10.1002/batt.202100260>

effective mechanical supports and simultaneously providing 1D electron conducting pathways.^[5] Si is deposited by a chemical vapor deposition (CVD)^[28] or sol-gel method^[29] on CNTs skeleton to obtain 1D Si-based hybrids. Although CNTs as robust conductive supports have obvious advantages in reducing the passive effects induced by the volume change and improving Si anode performance, the drawbacks of using CNTs are evident such as high cost and serious agglomeration. CNTs generally form stabilized bundles through van der Waal forces. It is hard to uniformly disperse the as-obtained Si/CNTs hybrid agglomerates in the electrode, resulting in losing the advantage of 1D Si-based nanostructures having good contact with conductive additives and binders. For another, 1D Si-based electrodes have been successfully prepared by magnesiothermic reduction of ordered mesoporous silica nanorods using amorphous carbon encapsulation^[30] and natural sepiolite.^[31] However, CVD synthesis method relies on the use of toxic and expensive Si precursors such as SiH_4 ^[28] or diphenylsilane,^[32] resulting in limiting the commercialization of Si-based anodes. Moreover, with the presence of carbon, inactive silicon carbide (SiC) layer tends to be formed due to a common reaction between Si and carbon, resulting in hindering lithium-ion diffusion into the Si phase and delivering poor electrochemical performance for Si-based electrodes. So far, for Si-based nanostructures engineering, magnesiothermic reduction has been considered as one of the scalable synthesis approaches at a low operating temperature ranging from 500 to 800 °C. As we know, bacterial cellulose (BC), a typical biomass material, is produced on industrial scales by bacteria gluconacetobacter xylinus in culture, which is composed of intrinsic cellulose nanofibers with high crystallinity and a diameter of 20–100 nm.^[33] It is increasingly being used as a strong structural template to synthesize active, functional BC for both biological and non-biological applications.^[34,35] This low-cost, eco-friendly and abundant BC possesses a unique nanofibrous structure, which can be converted into 1D carbon nanofibers through pyrolysis as a robust platform due to their high mechanical flexibility and good electrical conductivity.^[36,37] Furthermore, CO₂ as a typical and major greenhouse gas can cause global warming. Reducing CO₂ emissions is urgent and significant to address global warming issue. Consuming CO₂ can make up for the greenhouse gas emissions to accelerate carbon neutral. Thus, developing a facile and scalable fabrication of Si-based nanostructures with high battery performance is extremely challenging and important, so as to accelerate the commercialization of Si-based anodes for LIBs.

Herein, we fabricate novel 1D robust Si-based nanorods by employing pyrolytic BC (pBC) as 1D carbon skeleton and introducing CO₂ into magnesiothermic reduction reported by our recent studies.^[38,39] Carbon encapsulation of Si-based nanorods can be realized by transforming CO₂ into amorphous carbon in magnesiothermic reduction. Meanwhile, the presence of CO₂, a slightly oxidizing greenhouse gas, could reduce inactive SiC amount of the resultant Si-based composites. Very interestingly, during the pyrolytic synthesis process of SiO₂/pBC hybrids, a pBC self-assembled parallel arrangement phenomenon occurs, and then pBC arrays serve as a strong structure

stabilizer in the Si/C composites, which can maintain the initial nanorod morphology even without carbon encapsulation during violent magnesiothermic reduction and accelerate the formation of 1D robust Si-based nanorods with good dispersion. In addition, axial void spaces of the pBC arrays provide additional free surfaces to anchor Si nanoparticles. More significantly, pBC arrays robust support and CO₂-derived in-situ generated amorphous carbon encapsulation by virtue of their high mechanical strength, porous nature and good electronic conductivity endow the Si/C nanorods with high structure robustness and good flexibility to accommodate stress and volume changes of Si particles, and lithium-ion transportation kinetics during the charging and discharging processes, resulting in superior electrochemical performance. To be specific, Si-based nanorods anodes with carbon component content of 11 wt% exhibit high reversible capacities of 673 mAh g⁻¹ and capacity retention of 53.5% after 200 cycles at 0.5 Ag⁻¹ for LIBs.

Results and Discussion

In this study, carbon-encapsulated Si nanorods with pyrolytic BC arrays as 1D structure support were synthesized by using our previous CO₂-introduced magnesiothermic reduction method.^[38,39] To explore the formation mechanism of Si/C nanorods, morphologies and structures of the concerning samples are depicted as Figures 1 and S1. Bacterial cellulose hydrogels have an abundant three-dimensional (3D) porous cross-linked fiber structure, as presented in Figure S1(a). After pyrolysis at high temperature, the as-prepared pBC still kept 3D porous fibrous skeleton, which has been proved to have the advantages of outstanding mechanical properties.^[37] Meanwhile, benefiting from massive hydroxyl groups on the surface of BC, in situ generated SiO₂ nanoparticles can be adhered to its fiber surface homogeneously, shown in Figure S1(c). FT-IR spectrum of BC aerogels shows a broad peak between 3500 and 3300 cm⁻¹ in Figure S2, corresponding to the –OH stretching vibration, demonstrating massive hydroxyl groups on the surface of BC.^[40,41] The average diameter size of such porous interconnected SiO₂/BC fibers is 100–150 nm, 4 times larger than that of BC. After pyrolysis of SiO₂/BC composites with above 10 micrometers length, the cross-linked fiber framework breaks into short rods with less than 5 μm length and reconstructs to arrays with 300–400 nm width. Although the BC fibers are deoxidized and contracted obviously, SiO₂ layer on the surface has not any shrinkage in the longitudinal direction, resulting in the fibers breakage during the pyrolysis. The resultant fractured SiO₂/pBC fibers are more conducive to the following magnesiothermic reduction reaction. After CO₂-introduced magnesiothermic reduction, the as-obtained Si/pBC-CO₂ displays an initial nanorod structure. In addition, the Si nanoparticles agglomerate slightly on the surface of pBC, as shown in Figure 1(b). As we know, excessive Mg vapor reacts with CO₂ gas to form a new carbon layer deposited on the surface of the reduced Si nanoparticles. Meanwhile, it can promote the transformation from Mg₂Si to Si and Mg, which

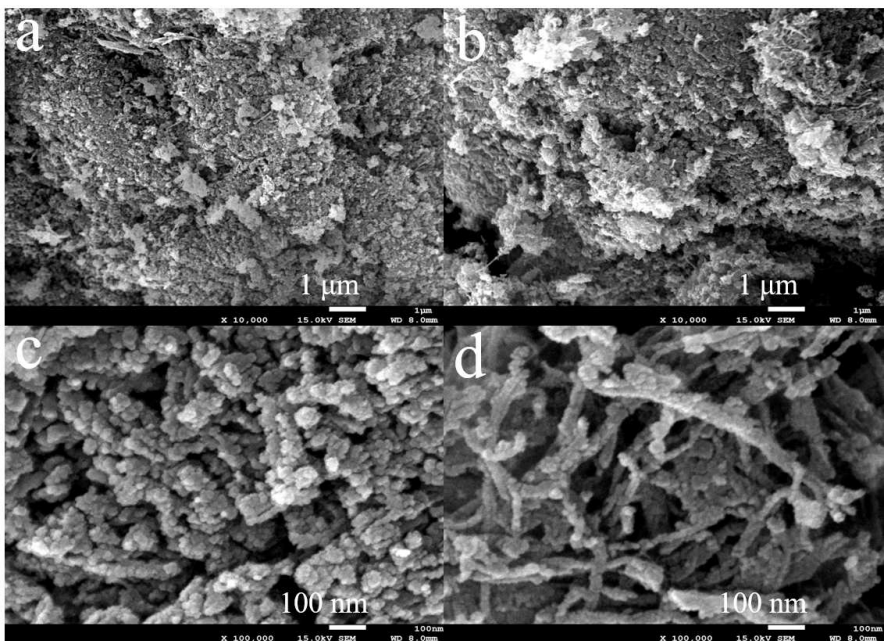


Figure 1. FE-SEM images of a) Si/pBC, b) Si/pBC-CO₂; the magnified images of c) Si/pBC, d) Si/pBC-CO₂.

has been explained in detail by our previous report.^[38] Attributed to the introduction of CO₂ in magnesiothermic reduction, the produced new carbon layer is beneficial for remaining the original 1D structure of Si/pBC-CO₂. By contrast, Si/pBC synthesized by using a traditional magnesiothermic reduction method shows an irregular small Si particles agglomeration in Figure 1(a), leading to the increased Si particles size and disappearance of nanorod structure. This phenomenon is mainly ascribed to loss of hydrogen bonds between Si and pBC arrays, making it unable to maintain the stability of the Si/pBC nanorod structure. For comparison, SiO₂ spheres prepared by using Stöber method^[42] are also reduced in traditional magnesiothermic reduction.^[43] The reduced and sintered Si particles basically present the spherical structure, shown in Figure S3(a and b).

Microstructures and morphologies of the Si/pBC-CO₂ sample were further characterized by TEM images in Figure 2. TEM results of the Si/pBC-CO₂ composite present a porous structure. Figure 2(a and b) shows that Si nanocrystals with an average particle size of 10 nm are uniformly distributed in the Si/pBC-CO₂ structure. The high-resolution TEM (HRTEM) images of Si/pBC-CO₂ demonstrate that 1D porous Si/C nanorods are successfully formed in Figure 2(c) and Si particles as cores are surrounded by naturally formed SiO_x inner-shell (~1.1 nm) and wrinkled and disordered carbon layers outer-shell (~4.5 nm), as shown in Figure 2(d). The lattice spacing of 0.31 nm corresponds to the (111) plane of Si crystals in Figure 2(d).

As depicted in Figure 3, XRD patterns of Si spheres are assigned to the cubic phase of Si (JPCDS 27-1402). For Si/pBC, distinct peaks of Si show weaker than those of Si spheres, consistent with previously reported literature.^[44] To the best of our knowledge, the Si extraction yield of SiO₂/C composites is lower than that of pristine SiO₂ during the conventional

magnesiothermic reduction.^[38] Si/pBC-CO₂ displays stronger characteristic peaks of Si, compared with Si/pBC synthesized without CO₂ introduced into magnesiothermic reduction, implying high Si yield, better crystallinity of Si and low Mg₂Si intermediate amount. This is because that the introduction of CO₂ in magnesiothermic reduction can not only accelerate the Si transformation from Mg₂Si, along with an improvement of Si extraction yield,^[45,46] but also lead to carbon deposition on the surface of nanorod structures, realizing carbon encapsulation of Si nanorods. Notably, inactive SiC component can be demonstrated in both Si/pBC and Si/pBC-CO₂ according to their XRD peaks.

To confirm the formation mechanism of carbon encapsulated Si nanorods, TGA analysis was further adopted to evaluate carbon content of SiO₂/pBC, Si/pBC and Si/pBC-CO₂ compounds and thermal stability of SiO₂/BC. As shown in Figure 4(a), SiO₂/BC composites undergo a large mass loss from 300 to 350 °C, corresponding to violent decomposition of BC component at air atmosphere, and remain 63 wt % of SiO₂. Besides, all the SiO₂/pBC, Si/pBC and Si/pBC-CO₂ composites display a mass decline in the temperature range of 300–650 °C, resulting from oxidation of carbon layer derived from CO₂. Notably, Si/pBC prepared through magnesiothermic reduction of SiO₂/pBC, has less carbon content of 3 wt %, compared with SiO₂/pBC (12 wt %). Thus, pBC loss obviously occurs due to the formation of inactive SiC component, which is demonstrated based on the XRD results mentioned above. Compared with Si/pBC, Si/pBC-CO₂ has larger carbon content of 11 wt %, resulting from carbon deposition and encapsulation from CO₂ transformation to maintain the nanorod structure during the magnesiothermic reduction process. As we know, Raman spectra were conducted to obtain carbon structural information. According to Raman spectra of SiO₂/pBC, Si/pBC and Si/pBC-CO₂ in Figure 4(b), two

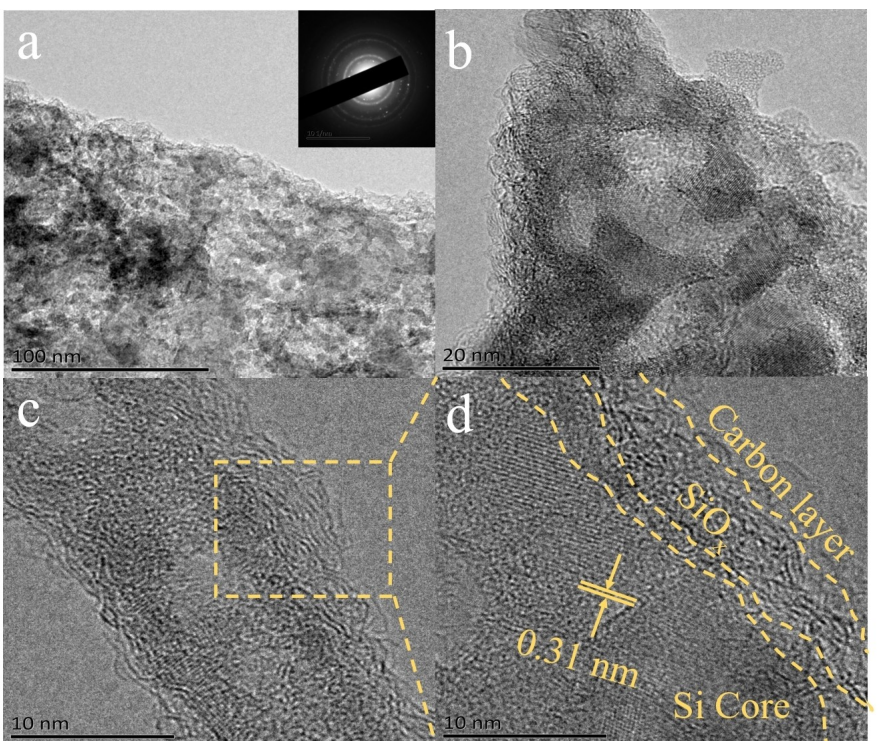


Figure 2. a) TEM (inset: selected area electron diffraction patterns) and b-d) HRTEM images of Si/pBC-CO₂.

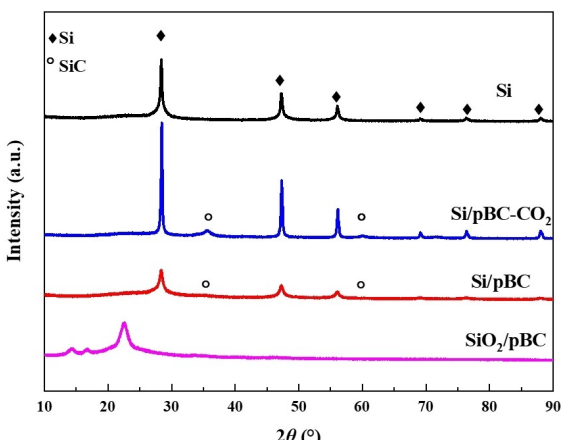


Figure 3. XRD patterns of Si, SiO₂/pBC, Si/pBC and Si/pBC-CO₂.

separated characteristic peaks of D-band and G-band at approximately 1360 and 1600 cm⁻¹ could be found, attributed to local defects or disordered amorphous carbon and graphite carbon, respectively.^[47] Si/pBC-CO₂ possesses the minimum band area ratio (I_D/I_G) of 1.9 among all the carbon-based hybrids in Figure 4(b), implying the best carbon crystallinity or graphitization degree, corresponding to a fast electron transport in the whole Si-based composites.^[25]

From nitrogen adsorption/desorption isotherms of SiO₂, Si, Si/pBC and Si/pBC-CO₂ in Figure S4, all the samples show apparent hysteresis at relatively high pressure ($P/P_0 = 0.8-1.0$), suggesting the existence of mesopores. Si spheres display a mesopore size of about 9 nm in Figure S4(b). Both Si/pBC and

Si/pBC-CO₂ are porous with a certain size distribution, as shown in Figure S4(c and d). The detailed specific surface area (SSA) and pore volume of SiO₂, Si, Si/pBC and Si/pBC-CO₂ are listed in Table 1. Si spheres synthesized from SiO₂ by using conventional magnesiothermic reduction, possess the largest SSA of 259.5 m² g⁻¹ and the corresponding pore volume of 0.9 cm³ g⁻¹. However, excessive large pore volume and SSA can enhance more SEI layer formation on the active materials and then decrease the initial Coulombic efficiency (CE) of the battery. In addition, Si/pBC gives SSA of 79.2 m² g⁻¹ and pore volume of 0.52 cm³ g⁻¹. Notably, the SSA of Si/pBC-CO₂ with its pore volume of 0.48 cm³ g⁻¹ is 120.8 m² g⁻¹, larger than that of Si/pBC, probably due to the fact that carbon derived from CO₂ in magnesiothermic reduction can prevent the Si nanoparticles agglomeration to some extent. Such large SSA and pore volume of Si/pBC-CO₂ are beneficial for the lithium-ion transport in the entire Si-based anodes.

The formation mechanism of carbon encapsulated Si nanorods with pBC arrays support in this study is proposed in Figure 5. Firstly, SiO₂ layers in situ grow homogeneously on the

Table 1. Specific surface area and pore volume of SiO₂, Si, Si/pBC and Si/pBC-CO₂.

Samples	BET surface area [m ² g ⁻¹]	Pore volume [cm ³ g ⁻¹]
SiO ₂	26.1	0.41
Si	259.5	0.90
Si/pBC	79.2	0.52
Si/pBC-CO ₂	120.8	0.48

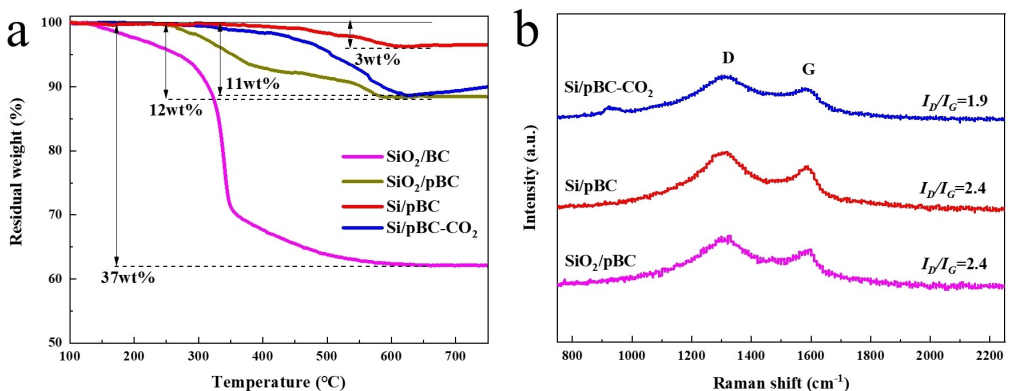


Figure 4. a) TG curves of SiO₂/BC, SiO₂/pBC, Si/pBC and Si/pBC-CO₂ under air atmosphere. b) Raman spectra of SiO₂/pBC, Si/pBC and Si/pBC-CO₂.

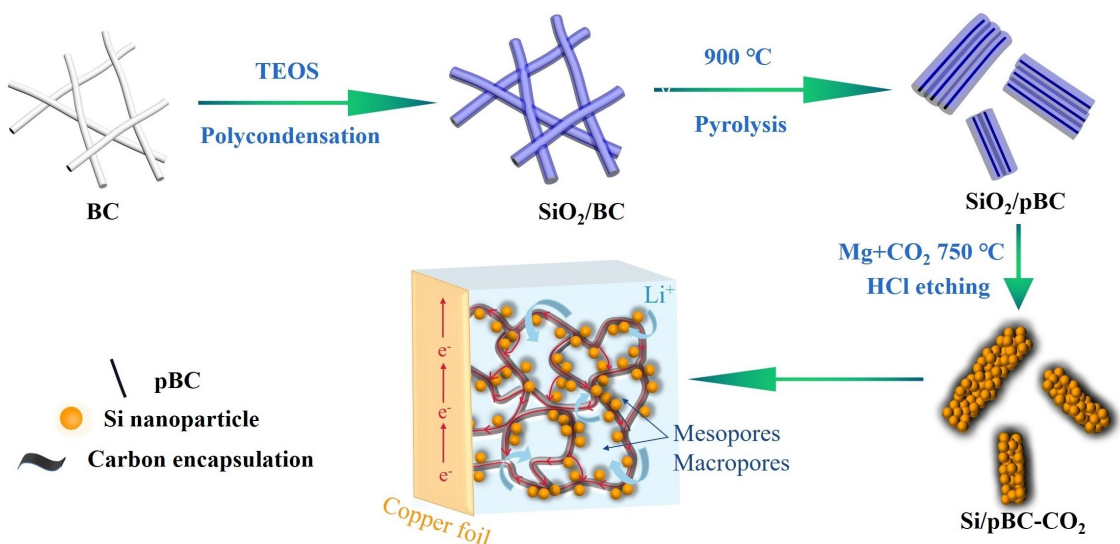


Figure 5. Schematic illustration of the silicon-based nanorods formation mechanism and the ionic and electronic transport mechanisms of Si/pBC-CO₂ electrodes.

surface of BC interconnected nanofibers, benefiting from their rich hydroxyl groups. Subsequently, SiO₂/BC membranes undergo the pyrolysis at high temperature of 900 °C to form pBC arrays-supported SiO₂ nanorods. After CO₂-introduced magnesiothermic reduction and the following HCl etching to remove MgO and MgSi₂ byproducts, the resultant Si/C nanorods possess highly stable and porous 1D architecture with a low specific surface area of 120.8 m² g⁻¹ and a large carbon component content of 11 wt%, in favor of its commercial application in practical LIBs. Ionic and electronic transportation pathways during the charging process is also shown in Figure 5. When lithium ions extract from Si cores and then transport through electrolyte owing to the existence of mesopores and macropores in the Si/pBC-CO₂ structure, electrons move quickly through the pBC skeleton and carbon layers on the surface of Si active particles to maintain the charge balance. The discharging process is reverse. Notably, pBC arrays-supported Si/pBC-CO₂ nanorods with carbon encapsulation by virtue of their large mechanical strength, porous nature and high electronic conductivity endow good accom-

mmodation of stress and volume changes, fast electron transfer and lithium-ion transportation pathways, which are conducive to superior rate performance and good cycling stability.

The surface chemical states of Si/pBC and Si/pBC-CO₂ composites were further analyzed by XPS analysis, shown in Figure 6. XPS survey spectra in Figure 6(a and d), display four characteristic peaks, ascribed to Si 2p, Si 2s, C 1s and O 1s.^[48] Compared with SiO₂/pBC and Si/pBC in Table S1, Si/pBC-CO₂ sample shows a relatively low oxygen content of 14.38 at%, which is obviously reduced, indicating that the introduction of CO₂ into magnesiothermic reaction can improve the SiO₂ reduction efficiency. According to the high-resolution Si 2p and C 1s spectra of SiO₂/pBC in Figure S5, no distinct peak of Si—C bond can be observed, suggesting that SiC component can not be formed during the pyrolysis process of SiO₂/BC composites. Moreover, the high-resolution Si 2p spectra of Si/pBC and Si/pBC-CO₂ in Figure 6(b and e) can be divided into six distinct peaks at 99.3, 99.9, 100.5, 101.4, 103.1 and 104 eV, corresponding to Si⁰2p^{3/2}, Si⁰2p^{1/2}, Si⁺, Si²⁺, Si³⁺ and Si⁴⁺, respectively.^[31] To be specific, Si²⁺ mainly originates from SiC. The high-resolution

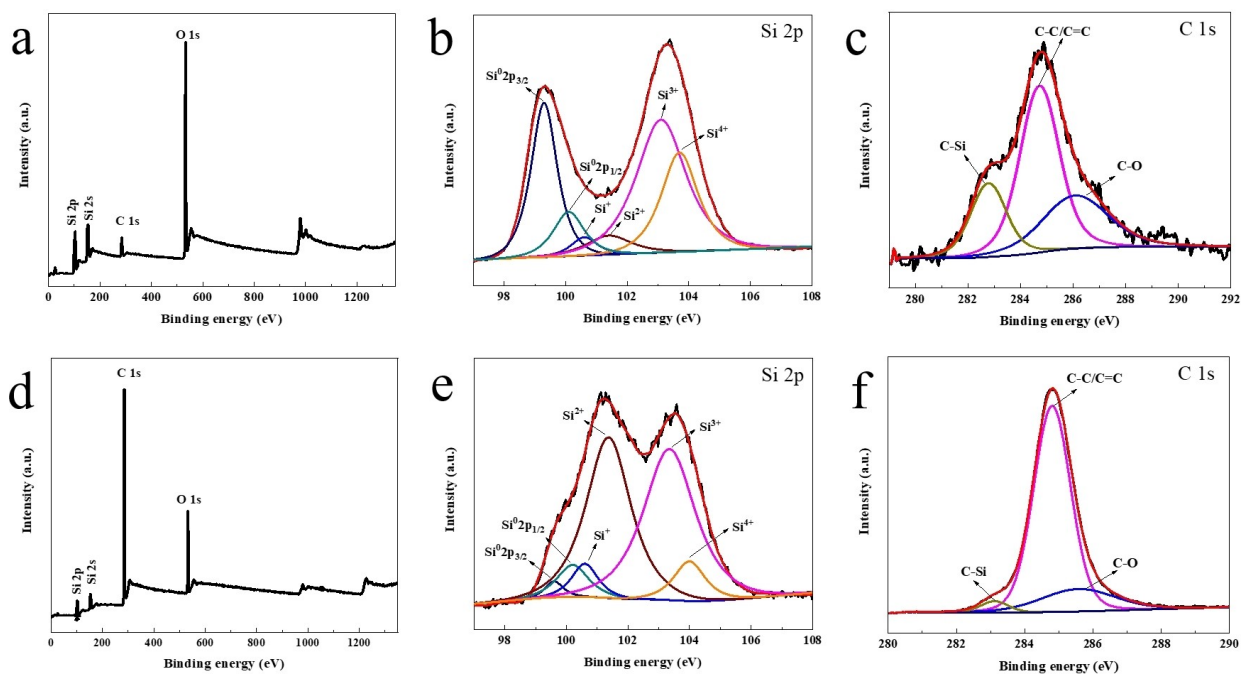


Figure 6. XPS survey spectra: a) Si/pBC and d) Si/pBC-CO₂; high resolution Si 2p XPS spectra: b) Si/pBC and e) Si/pBC-CO₂; high resolution C 1s XPS spectra: c) Si/pBC and f) Si/pBC-CO₂.

C 1s spectra of Si/pBC and Si/pBC-CO₂ in Figure 6(c and f) exhibit three distinct peaks located at 283, 284.7 and 285.8 eV, which link with the C–Si, C–C/C=C, and C–O groups, respectively,^[49] indicating the existence of inactive SiC component, consistent with the above XRD results. It is common that SiC material is easy to form during magnesiothermic reduction process when the SiO₂ precursor contains carbon component. Notably, after introducing CO₂ into magnesiothermic reduction reaction, surface carbon atom amount of Si/pBC-CO₂ is quantified as high as 73.61 at%, higher than that of Si/pBC (36.8 at%) in Table S1, and Si²⁺ surface concentration of Si/pBC-CO₂ is up to 38.74 at% in Table S2. Based on carbon element fitted results of high resolution XPS spectrum of C 1s listed in Table S3, Si/pBC and Si/pBC-CO₂ possess SiC amount of around 7.05 at% and 2.17 at%, respectively. Thus, introducing CO₂ into magnesiothermic reduction can inhibit the formation of inactive SiC. For Si/pBC-CO₂, Si nanorods are surrounded with the generated massive carbon, slight SiC and SiO_x components to maintain their structure stability.

To further assess the electrochemical performance, CV curves of Si, Si/pBC and Si/pBC-CO₂ electrodes were collected between 0.01 and 1.5 V for first five cycles, exhibited in Figure 7(a–c). During the first discharge process, Si, Si/pBC and Si/pBC-CO₂ electrodes show an irreversible wide peak of 0.4–1.2 V, suggesting the formation of SEI films and the decomposition of electrolyte, and a reductive peak below 0.1 V, mainly attributed to the phase transition from crystalline Si to amorphous Li_xSi.^[50] Subsequently, during the charging process, two cathode peaks at 0.32 and 0.54 V suggest the dealloying process from Li_xSi to amorphous Si. In the second cycle, Si and Si/pBC-CO₂ electrodes deliver a reversible broad peak at 0.19 V in Figure 7(a and c), which is attributed to the lithiation of

amorphous Si. However, Si/pBC anode has not such obvious peak in Figure 7(b), due to its low active Si content. Two cathode peaks situated at 0.32 and 0.54 V, and anode peak located at 0.2 V remain in the next few cycles, showing high reversibility. Additionally, the current intensities of the aforementioned reversible anodic and cathodic peaks gradually increase with cycles. This is a typical phenomenon of crystalline Si-based lithium-ion battery anode, which is related to deeper activation reactions between active materials and lithium ions. Moreover, Si, Si/pBC and Si/pBC-CO₂ anodes in Figure 7(d–f) show charging and discharging curves in the first three cycles at 100 mAg⁻¹. The initial discharging/charging capacities of Si, Si/pBC and Si/pBC-CO₂ electrodes are 1797/835, 1526/638 and 1462/859 mAh g⁻¹ with the initial CE of 46.5%, 41.8% and 58.7%, respectively. After the first cycle, discharge capacities of Si, Si/pBC and Si/pBC-CO₂ electrodes in the following cycles stabilize at 993, 756, and 1011 mAh g⁻¹, respectively. Besides, the CE of Si, Si/pBC and Si/pBC-CO₂ electrodes in the third cycle increase to 88.1%, 89.4% and 91.1%, respectively. Notably, the charging and discharging curves in the next cycles almost overlap, suggesting relatively good stability.

The rate capability of Si, Si/pBC and Si/pBC-CO₂ electrode was further studied at different current densities from 0.1 to 2 A g⁻¹ in Figure 8(a). The discharging capacities of Si/pBC-CO₂ electrode after activation at 0.1, 0.2, 0.5, 1 and 2 A g⁻¹ are 880, 791, 673, 531 and 397 mAh g⁻¹, respectively. With the increasing current density from 0.1 to 2 A g⁻¹, discharging capacities of Si/pBC-CO₂ electrode drop slightly, indicating a good power characteristic. When the current density reduces to 0.1 A g⁻¹, its discharge capacity returns to 787 mAh g⁻¹ with capacity retention of 89.5%. Si electrode exhibits the highest discharge capacity of 946 mAh g⁻¹ at 0.1 A g⁻¹. However, its discharge

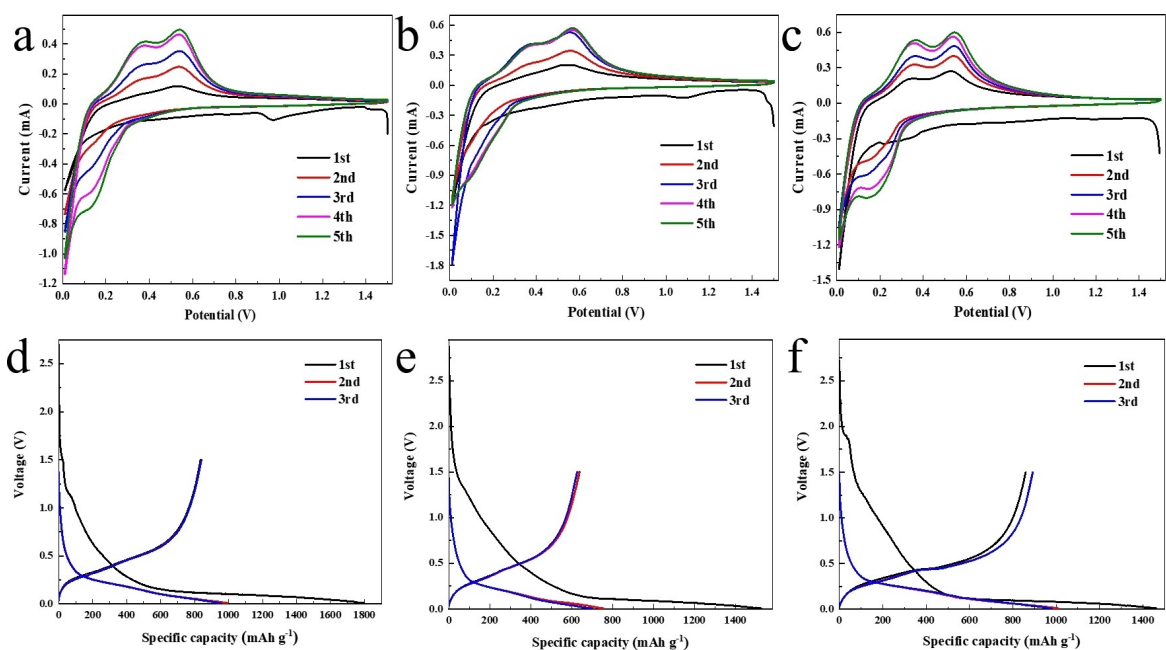


Figure 7. CV curves at a scan rate of 0.1 mV s^{-1} between 0.01 and 1.5 V : a) Si, b) Si/pBC and c) Si/pBC- CO_2 ; charging-discharging curves at 100 mA g^{-1} for the initial three cycles: d) Si, e) Si/pBC and f) Si/pBC- CO_2 .

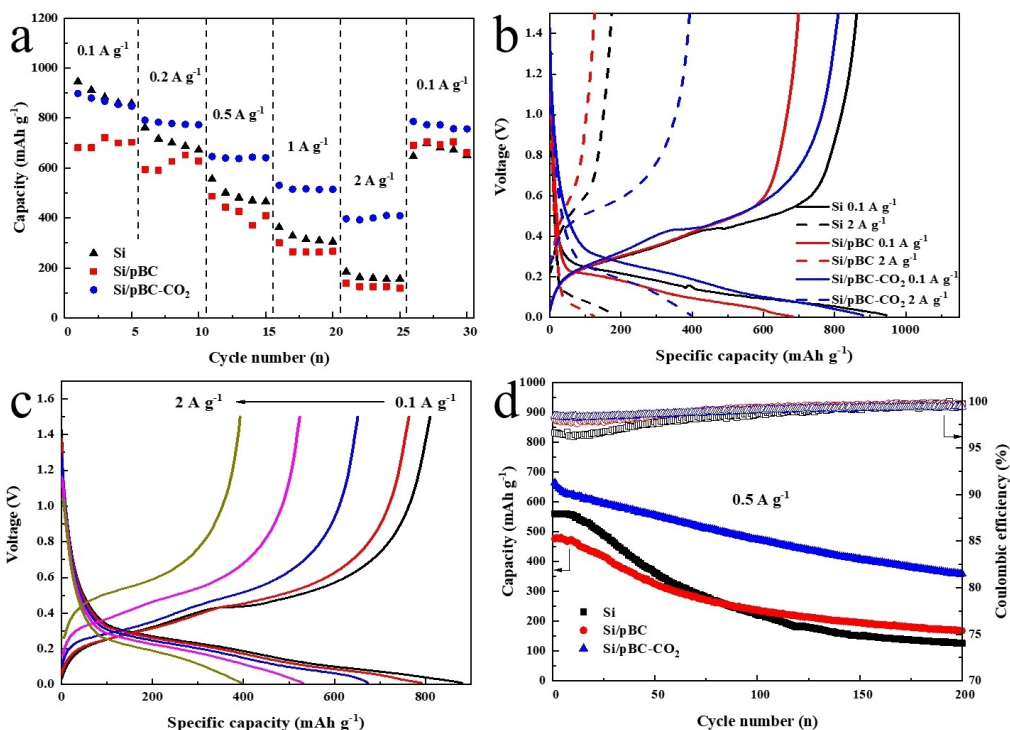


Figure 8. Electrochemical performances of Si, Si/pBC and Si/pBC- CO_2 electrodes. a) rate capability at various current densities from 0.1 to 2 A g^{-1} ; b) galvanostatic discharging-charging curves at 0.1 and 2 A g^{-1} from 0.01 to 1.5 V ; c) galvanostatic charging-discharging curves of the Si/pBC- CO_2 electrode at various current densities from 0.1 to 2 A g^{-1} ; d) cycling performance at 0.5 A g^{-1} between 0.01 and 1.5 V .

capacity reduces rapidly when the current density increases from 0.2 to 2 A g^{-1} , corresponding to 700 , 557 , 314 and 159 mAh g^{-1} , respectively. Compared with Si and Si/pBC- CO_2 anodes, Si/pBC anode possesses worse discharge capacities of 681 , 594 , 487 , 263 and 125 mAh g^{-1} at 0.1 , 0.2 , 0.5 , 1 and

2 A g^{-1} , respectively. Figure 8(b) shows the galvanostatic charging-discharging curves of three electrodes after activation. At 0.1 A g^{-1} , both charging curves of Si and Si/pBC- CO_2 electrodes show an obvious voltage platform at about 0.4 V , suggesting the dealloying reaction of amorphous Li_xSi . However, for Si/pBC

electrode, there is no obvious charging platform at around 0.4 V, due to poor Si crystallinity and low active Si amount in the Si/pBC hybrid based on the XRD results. In addition, the discharge voltage slope between 0.01 and 0.28 V corresponds to the alloying reaction of amorphous Si. Notably, according to charging curves at 0.1 A g^{-1} in Figure 8(b), both Si/pBC and Si/pBC-CO₂ electrodes have no obvious carbon reaction with lithium ions, consistent with CV results in Figure 7, so it can be speculated that Si/pBC and Si/pBC-CO₂ anodes with relatively low carbon material amount of 3 wt% and 11 wt%, respectively, possess extremely limited capacity contribution of carbon. Besides, compared with Si and Si/pBC electrodes, the gap between the charging and discharging platforms of Si/pBC-CO₂ electrode at 2 A g^{-1} is the smallest, suggesting the minimum polarization, which is mainly ascribed to large carbon component amount, strong pBC arrays support and good carbon encapsulation of Si/pBC-CO₂, maintaining the stability of 1D rod-like nanostructure. As presented in Figure 8(c), for Si/pBC-CO₂ anode after activation, charging/discharging capacities at 0.1, 0.2, 0.5, 1 and 2 A g^{-1} are 811/880, 764/791, 655/673, 524/531 and 393/397 mAh g⁻¹ with CE of 92.2%, 96.6%, 97.3%, 98.7% and 99.0%, respectively. Such excellent rate performance of Si/pBC-CO₂ is attributed to its unique 1D rod-like nanostructure, high Si content, relatively large specific surface and pore volume, and superior carbon properties with large mechanical strength, high electronic conductivity, and attractive carbon networks consisting of pBC arrays and amorphous carbon encapsulation, which are beneficial to enhance lithium-ion transportation kinetics and electrolyte wetting influences, and also accommodate Si volume change.

Figure 8(d) shows cycling performances at 0.5 A g^{-1} for Si, Si/pBC and Si/pBC-CO₂ electrodes after activation. The discharge capacity of Si decreases dramatically from 557 to 125 mAh g⁻¹ with cycling, along with a low capacity retention of 22.4%. Compared with Si electrode, Si/pBC electrode has only 487 mAh g⁻¹ of the discharge capacity and 35.4% of capacity retention after 200 cycles. Few can deny the fact that carbon component can stabilize the interface between electrolyte and Si and maintain such unique nanorod architecture and relieve the volume change of Si-based anodes for LIBs. It is obvious to see that with the rising carbon component amount in Si-based compounds, cycling performance is significantly enhanced. As presented in Figure 8(d), Si/pBC-CO₂ electrode depicts the best cycling performance, compared with Si and Si/pBC electrodes. Its discharge reversible capacity decreases slowly from 673 to 360 mAh g⁻¹ after 200 cycles. The corresponding capacity retention is 53.5%, related to a slight decrease of about 0.27% for each cycle, indicating improved cycling stability resulting from superior carbon properties and unique porous nanorod architecture of Si/pBC-CO₂. After 200 cycles, the CE of Si/pBC-CO₂ electrode is nearly 100%. Thus, Si/pBC-CO₂ electrode has excellent rate capability and good cycling performance owing to its unique Si/C nanorods architecture composed of Si nanoparticles with good crystallinity, slight inactive SiC component and versatile carbon materials as pBC arrays support and carbon encapsulation, which can be conductive to better volume change and

mechanical stress during the charging and discharging processes. Moreover, carbon component with high electronic conductivity provides fast electron transportation paths and benefits to electron transfer in the Si/pBC-CO₂ anodes.

Figure S6 shows typical EIS of Si, Si/pBC and Si/pBC-CO₂ electrodes before cycling and after 50 cycles at 0.4 V. As presented in Figure S6(a), the Nyquist plots of Si, Si/pBC and Si/pBC-CO₂ electrodes before cycling exhibit a depressed semicircle in the high-middle frequency region and a straight line in the low frequency region. As we know, the Nyquist semicircle is connected with SEI films resistance (R_{SEI}) and charging transfer resistance (R_{ct}), while the sloped line is assigned to lithium-ion diffusion behavior.^[51] Compared with Si/pBC and Si/pBC-CO₂ electrodes, pure Si electrodes before cycling have the largest semicircle radius in the high-middle frequency regions, connected with high R_{ct} and R_{SEI} values, implying the maximum polarization. After 50 cycles, for Si and Si/pBC-CO₂ electrodes, the semicircle radius reduces, mainly due to more active Si reacted with lithium ions when cycling. However, Si/pBC electrode exhibits larger semicircle radius after 50 cycles than before cycling, which is probably because that the agglomeration of Si particles without carbon encapsulation in the Si/pBC hybrid occurs.

Conclusion

To summarize, we have explored the usage of biomass bacterial cellulose derived carbon skeleton for Si nanorods. pBC arrays formed through self-assembled parallel arrangement during the SiO₂/BC pyrolytic process, serve as a strong structure stabilizer in the Si/C hybrids. Besides, introducing CO₂ as extra carbon source into traditional magnesiothermic reduction reaction can realize in-situ construction of 1D robust porous Si/C nanorods through carbon encapsulation and inhibit the SiC generation to some extent. Furthermore, carbon-encapsulated Si nanorods anodes with pyrolytic BC arrays as 1D structure support demonstrate a high reversible discharge capacity of 880.1 mAh g⁻¹ at 0.1 A g^{-1} and 673 mAh g⁻¹ at 0.5 A g^{-1} . In addition, they also deliver superior capacity retention (0.5 A g^{-1}) of 53.5% after 200 cycles for LIBs. Such high lithium storage capacity, superior rate capability and excellent cycling stability for Si/C nanorods anodes are attributed to unique porous 1D architecture and superior carbon properties originating from pBC arrays support and CO₂ derived amorphous carbon layer by virtue of high electronic conductivity and good mechanical property, which can endow the Si-based nanorods with good accommodation of stress and volume changes, a high structure robustness and superior lithium ions transportation and electrons transfer kinetics. More significantly, in this work, renewable biomaterials derived Si/C nanorods synthetic approach possesses the merits of low cost and scalability, probably accelerates Si-based anodes for commercialized application in the next generation LIBs.

Experimental Section

Fabrication of SiO₂/BC composites

The BC pellicles were firstly immersed in 0.25 M NaOH solution, washed with deionized water for several times to remove bacteria, and then cut into 4×4 cm rectangular hydrogels. After squeezed to remove redundant water, BC thin hydrogels were soaked into the mixture of deionized water, ethanol, and tetraethyl orthosilicate (TEOS) in a 1:4:0.8 volume ratio. Subsequently, these hydrogels were immersed in ammonia solution (28 wt%) for 12 h at room temperature. After washed with deionized water for several times and subjected to freeze-drying, SiO₂/BC composites were obtained, denoted as SiO₂/BC.

Fabrication of Si and Si/C composites

SiO₂/BC composites were annealed at 400 °C for 2 h, and further heated to 900 °C for 1 h to obtain SiO₂/pBC samples under Ar atmosphere. Subsequently, these SiO₂/pBC samples were uniformly mixed with Mg and MgO powders at a weight ratio of 1:1:4. The mixture was reduced at 750 °C under Ar atmosphere for the first four hours and then under a mixed gases of Ar and CO₂ at a volume ratio of 6:5 for the following four hours. At last, the products were washed with 1 M HCl (molar ratio of ethanol:H₂O:HCl=8.86:4.75:0.67) solution and stirred for 12 h to remove the MgO and Mg₂Si byproducts, marked as Si/pBC-CO₂. By contrast, sample Si/pBC were obtained only under Ar atmosphere for 8 h by using the same conditions as Si/pBC-CO₂. Meanwhile, Si nanospheres were synthesized from SiO₂ nanospheres obtained by a typical Stöber synthesis^[42] by using the same conditions as Si/pBC.

Characterization

The morphologies of materials were measured by field emission scanning electron microscopy (FE-SEM, Hitachi S-4800) and transmission electron microscopy (TEM, JEM-2100). X-ray diffraction (XRD) patterns from 10° to 90° were recorded with Cu K_α radiation ($\lambda = 1.5405 \text{ \AA}$). Thermogravimetric analysis (TGA) tests were performed under air atmosphere. Raman spectra were obtained at an excitation wavelength of 514 nm by an Ar-ion laser. The surface area by the Brunauere-Emmette-Teller (BET) method and pore distribution by the Barrett-Joyner-Halenda (BJH) method were calculated by Micrometrics ASAP 2010 analyzer (Quantachrome Instruments, USA). The surface chemical states were carried out by the X-ray photoelectron spectra (XPS) measurement on a ESCALAB 250Xi spectrometer.

Electrochemical measurements

The electrochemical performance was investigated in the CR2032 coin cells. The active material, carbon black, styrene-butadiene rubber (SBR) and sodium carboxymethyl cellulose (CMCNa) were stirred in deionized water for 8 h at a mass ratio of 6:2:1:1 to obtain a uniform and viscous mixture. The paste was coated on a copper foil and vacuum-dried at 65 °C for 10 h. The dried foil was cut into discs as working electrodes and active material mass loading was 2 mg cm⁻². The liquid electrolyte was 1 M LiPF₆ in ethylene carbonate/dimethyl carbonate/fluoroethylene carbonate (EC/DMC/FEC, 45:45:10 v/v). Galvanostatic charge-discharge tests were carried out on a LAND battery test system in a voltage window between 0.01 and 1.5 V (vs. Li/Li⁺). Cyclic voltammetry (CV) was measured by a CHI760E electrochemical workstation with a scan rate of 0.1 mV s⁻¹ from 0.01 to 1.5 V. In addition, electro-

chemical impedance spectroscopies (EIS) were carried out in the frequency range from 0.01 to 100 kHz at 5 mV amplitude.

Acknowledgements

The work was supported by National Key Research and Development Program of China (grant number 2019YFB1503804), National Natural Science Foundation of China (grant number 21706135) and Priority Academic Program Development of Jiangsu Higher Education Institutions.

Conflict of Interest

The authors declare no conflict of interest.

Keywords: anode; CO₂ • lithium-ion batteries • pyrolytic bacterial cellulose • Si nanorod

- [1] H. J. Peng, J. Q. Huang, X. B. Cheng, Q. Zhang, *Adv. Energy Mater.* **2017**, 7, 1770141.
- [2] S. Choi, T.-w. Kwon, A. Coskun, J. W. Choi, *Science* **2017**, 357, 279–283.
- [3] Y. Wen, H. Zhang, *ChemSusChem* **2020**, 13, 3887–3892.
- [4] Q. Wang, T. Meng, Y. Li, J. Yang, B. Huang, S. Ou, C. Meng, S. Zhang, Y. Tong, *Energy Storage Mater.* **2021**, 39, 354–364.
- [5] X. Zhang, D. Kong, X. Li, L. Zhi, *Adv. Funct. Mater.* **2019**, 29, 1806061.
- [6] M. Salah, P. Murphy, C. Hall, C. Francis, R. Kerr, M. Fabretto, *J. Power Sources* **2019**, 414, 48–67.
- [7] S. Chen, L. Shen, P. A. van Aken, J. Maier, Y. Yu, *Adv. Mater.* **2017**, 29, 1605650.
- [8] Y. Yao, M. T. McDowell, I. Ryu, H. Wu, N. Liu, L. Hu, W. D. Nix, Y. Cui, *Nano Lett.* **2011**, 11, 2949–2954.
- [9] C. K. Chan, H. Peng, G. Liu, K. McIlwrath, X. F. Zhang, R. A. Huggins, Y. Cui, *Nat. Nanotechnol.* **2008**, 3, 31–35.
- [10] T. Song, J. Xia, J.-H. Lee, D. H. Lee, M.-S. Kwon, J.-M. Choi, J. Wu, S. K. Doo, H. Chang, W. I. Park, *Nano Lett.* **2010**, 10, 1710–1716.
- [11] H. Wu, G. Chan, J. W. Choi, I. Ryu, Y. Yao, M. T. McDowell, S. W. Lee, A. Jackson, Y. Yang, L. Hu, *Nat. Nanotechnol.* **2012**, 7, 310–315.
- [12] Q. Li, R. Cao, J. Cho, G. Wu, *Adv. Energy Mater.* **2014**, 4, 1301415.
- [13] H. Kim, B. Han, J. Choo, J. Cho, *Angew. Chem. Int. Ed.* **2008**, 47, 10151–10154.
- [14] B. Wang, X. Li, B. Luo, L. Hao, M. Zhou, X. Zhang, Z. Fan, L. Zhi, *Adv. Mater.* **2015**, 27, 1526–1532.
- [15] Y. Zhang, K. Hu, J. Ren, Y. Wu, N. Yu, A. Feng, Z. Huang, Z. Jia, G. Wu, *Dalton Trans.* **2019**, 48, 17683–17690.
- [16] P. Nie, Z. Le, G. Chen, D. Liu, X. Liu, H. B. Wu, P. Xu, X. Li, F. Liu, L. Chang, *Small* **2018**, 14, 1800635.
- [17] S. Yoo, J.-l. Lee, S. Ko, S. Park, *Nano Energy* **2013**, 2, 1271–1278.
- [18] B. Yang, X. Mao, S. Yang, Y. Li, Y. Wang, M. Wang, W. Deng, K. Han, *ACS Appl. Mater. Interfaces* **2016**, 8, 19587–19592.
- [19] H. Wu, G. Yu, L. Pan, N. Liu, M. T. McDowell, Z. Bao, Y. Cui, *Nat. Commun.* **2013**, 4, 1–6.
- [20] Y. You, X.-L. Wu, Y.-X. Yin, Y.-G. Guo, *Energy Environ. Sci.* **2014**, 7, 1643–1647.
- [21] K. Feng, M. Li, W. Liu, A. G. Kashkooli, X. Xiao, M. Cai, Z. Chen, *Small* **2018**, 14, 1702737.
- [22] S. W. Lee, M. T. McDowell, L. A. Berla, W. D. Nix, Y. Cui, *Proc. Nat. Acad. Sci.* **2012**, 109, 4080–4085.
- [23] X. Chen, H. Li, Z. Yan, F. Cheng, J. Chen, *Sci. China Mater.* **2019**, 62, 1515–1536.
- [24] M. Mandal, M. Kruk, *Chem. Mater.* **2012**, 24, 123–132.
- [25] X. Huang, J. Yang, S. Mao, J. Chang, P. B. Hallac, C. R. Fell, B. Metz, J. Jiang, P. T. Hurley, J. Chen, *Adv. Mater.* **2014**, 26, 4326–4332.
- [26] B. Gerisioglu, A. Ahmadivand, N. Pala, J. Lightwave Technol. **2017**, 35, 4961–4966.
- [27] J. K. Yoo, J. Kim, Y. S. Jung, K. Kang, *Adv. Mater.* **2012**, 24, 5452–5456.

- [28] R. Epur, M. Ramanathan, M. K. Datta, D. H. Hong, P. H. Jampani, B. Gattu, P. N. Kumta, *Nanoscale* **2015**, *7*, 3504–3510.
- [29] R. Liu, C. Shen, Y. Dong, J. Qin, Q. Wang, J. Icozzia, S. Zhao, K. Yuan, C. Han, B. Li, *J. Mater. Chem. A* **2018**, *6*, 14797–14804.
- [30] F.-H. Du, Y. Ni, Y. Wang, D. Wang, Q. Ge, S. Chen, H. Y. Yang, *ACS Nano* **2017**, *11*, 8628–8635.
- [31] Q. Chen, R. Zhu, S. Liu, D. Wu, H. Fu, J. Zhu, H. He, *J. Mater. Chem. A* **2018**, *6*, 6356–6362.
- [32] S. Karuppiah, C. Keller, P. Kumar, P.-H. Jouneau, D. Aldakov, J.-B. Ducros, G. Lapertot, P. Chenevier, C. Haon, *ACS Nano* **2020**, *14*, 12006–12015.
- [33] Z.-Y. Wu, H.-W. Liang, L.-F. Chen, B.-C. Hu, S.-H. Yu, *Acc. Chem. Res.* **2016**, *49*, 96–105.
- [34] M. C. DeRosa, C. Monreal, M. Schnitzer, R. Walsh, Y. Sultan, *Nat. Nanotechnol.* **2010**, *5*, 91.
- [35] S. Ye, L. Jiang, J. Wu, C. Su, C. Huang, X. Liu, W. Shao, *ACS Appl. Mater. Interfaces* **2018**, *10*, 5862–5870.
- [36] Z. Y. Wu, C. Li, H. W. Liang, J. F. Chen, S. H. Yu, *Angew. Chem.* **2013**, *125*, 2997–3001; *Angew. Chem. Int. Ed.* **2013**, *52*, 2925–2929.
- [37] X. Xu, J. Zhou, D. H. Nagaraju, L. Jiang, V. R. Marinov, G. Lubineau, H. N. Alshareef, M. Oh, *Adv. Funct. Mater.* **2015**, *25*, 3193–3202.
- [38] J. Zhang, S. Zuo, Y. Wang, H. Yin, Z. Wang, J. Wang, *J. Power Sources* **2021**, *495*, 229803.
- [39] J. Wang, Y. Wang, Q. Jiang, J. Zhang, H. Yin, Z. Wang, J. Gao, Z. Wu, J. Liang, S. Zuo, *Energy Fuels* **2021**, *35*, 10241–10249.
- [40] Y. Zhang, Y. Chen, X. Li, M. Alfred, D. Li, F. Huang, Q. Wei, *J. Power Sources* **2021**, *482*, 228963.
- [41] M. P. Illa, C. S. Sharma, M. Khandelwal, *Mater. Today Chem.* **2021**, *20*, 100439.
- [42] W. Stöber, A. Fink, E. Bohn, *J. Colloid Interface Sci.* **1968**, *26*, 62–69.
- [43] C. Real, M. D. Alcalá, J. M. Criado, *J. Am. Ceram. Soc.* **1996**, *79*, 2012–2016.
- [44] S. Guo, X. Hu, Y. Hou, Z. Wen, *ACS Appl. Mater. Interfaces* **2017**, *9*, 42084–42092.
- [45] Y. Zhang, N. Du, Y. Chen, Y. Lin, J. Jiang, Y. He, Y. Lei, D. Yang, *Nanoscale* **2018**, *10*, 5626–5633.
- [46] J. Entwistle, A. Rennie, S. Patwardhan, *J. Mater. Chem. A* **2018**, *6*, 18344–18356.
- [47] A. C. Ferrari, *Solid State Commun.* **2007**, *143*, 47–57.
- [48] Y. Li, L. Liu, X. Liu, Y. Feng, B. Xue, L. Yu, L. Ma, Y. Zhu, Y. Chao, X. Wang, *Mater. Chem. Phys.* **2021**, *262*, 124331.
- [49] J. Wang, R. Ran, J. Sunarso, C. Yin, H. Zou, Y. Feng, X. Li, X. Zheng, J. Yao, *J. Power Sources* **2017**, *347*, 259–269.
- [50] Z. Jiao, Y. Gao, S. Liu, S. Huang, Y. Jiang, Z. Chen, B. Zhao, *Electrochim. Acta* **2018**, *283*, 1702–1711.
- [51] T.-F. Yi, P.-P. Peng, Z. Fang, Y.-R. Zhu, Y. Xie, S. Luo, *Compos. B. Eng.* **2019**, *175*, 107067.

Manuscript received: September 15, 2021

Revised manuscript received: November 20, 2021

Version of record online: January 11, 2022